Song *et al. Energy Mater.* **2025**, *5*, 500139
DOI: 10.20517/energymater.2025.96

Energy Materials

Article

Open Access

Hierarchically porous two-dimensional Fe/N-codoped carbon nanoleaves for enhanced mass transfer and electrocatalytic oxygen reduction reaction

Limin Song[#], Yining Liu[#], Jing-Jing Wang, Ruotong Wu, Jing-Shuang Dang[*], Hang Zhang[*], Wei Zhang, Rui Cao, Haoquan Zheng[*]

Key Laboratory of Applied Surface and Colloid Chemistry, Ministry of Education, School of Chemistry and Chemical Engineering, Shaanxi Normal University, Xi'an 710119, Shaanxi, China.
[#]Authors contributed equally.

[*]**Correspondence to:** Prof. Haoquan Zheng, Assoc. Prof. Hang Zhang, and Assoc. Prof. Jing-Shuang Dang, Key Laboratory of Applied Surface and Colloid Chemistry, Ministry of Education, School of Chemistry and Chemical Engineering, Shaanxi Normal University, No. 620, West Chang'an Avenue, Chang'an District, Xi'an 710119, Shaanxi, China. E-mail: zhenghaoquan@snnu.edu.cn; zhangteacher@snnu.edu.cn; dangjs@snnu.edu.cn

How to cite this article: Song, L.; Liu, Y.; Wang, J. J.; Wu, R.; Dang, J. S.; Zhang, H.; Zhang, W.; Cao, R.; Zheng, H. Hierarchically porous two-dimensional Fe/N-codoped carbon nanoleaves for enhanced mass transfer and electrocatalytic oxygen reduction reaction. *Energy Mater.* **2025**, *5*, 500139. https://dx.doi.org/10.20517/energymater.2025.96

Received: 9 Jun 2025 **First Decision:** 25 Jun 2025 **Revised:** 8 Jul 2025 **Accepted:** 21 Jul 2025 **Published:** 13 Aug 2025

Academic Editor: Jiazhao Wang **Copy Editor:** Ping Zhang **Production Editor:** Ping Zhang

Abstract

Zinc-air batteries are promising energy conversion devices with high theoretical energy density, but their practical performance is limited by the kinetically sluggish oxygen reduction reaction kinetics at the air electrode. This kinetic bottleneck stems from the inefficient mass transport and insufficient accessible active sites. In order to solve this problem, constructing porous structure at the air electrode could be an efficient strategy to improve mass transfer and expose more active sites. Herein, we successfully constructed hierarchical porous structure with mesopores and micropores in two-dimensional (2D) Fe/N-codoped carbon nanoleaves. F127 micelles on the surface were introduced for the formation of mesopores, while microporous structure came from 2D Fe-doped Zeolitic Imidazolate Framework-L (ZIF-L) precursors. After pyrolysis in Ar, the derived 2D meso/microporous Fe/N-codoped carbon nanoleaves possess atomically dispersed Fe-N_x sites. Kinetic experiments demonstrate that the hierarchical porous structure reduces the mass transfer resistance. Furthermore, density functional theory calculations reveal that the Fe-N_x active sites with concave curvature within the hierarchical porous structure can lower the *OH binding energy, thereby enhancing the oxygen reduction reaction activity. The nanostructure-engineered fabrication of this hierarchical porous structure is critical for accelerating mass transfer, ultimately maximizing the efficiency of active sites.

Keywords: Hierarchically porous material, mass transfer, single atom, oxygen reduction reaction, Zn-air battery

INTRODUCTION

In recent years, rising global energy demand and growing environmental concerns have spurred extensive research into sustainable energy development and advanced storage technologies. To date, various clean energy sources (e.g., solar, wind, and tidal) and storage devices (e.g., fuel cells, lithium-ion, and metal-air batteries) have been developed[1-4]. Among these, zinc-air batteries (ZABs) have garnered scientific interest due to their low environmental impact, high energy density, and cost-effectiveness. Although traditional Pt-based electrocatalysts can efficiently drive the 4e$^-$ oxygen reduction reaction (ORR), their large-scale application is hindered by high cost and poor poisoning resistance[5-8]. In contrast, Fe, N codoped carbon (Fe/NC) electrocatalysts benefit from atomically dispersed Fe-N_x sites and the carbon supports, demonstrating high intrinsic activity and anti-poisoning capability[9-11]. However, in ZABs, a thick diffusion layer forms on the air electrode surface, impeding the rapid O_2 diffusion, water release during ORR, and the diffusion rate of OH^- during oxygen evolution reaction (OER)[12-14]. These challenges underscore the sensitivity of electrodes to the local microenvironment under real operating conditions, emphasizing the need for greater exposure of active sites and enhanced mass transfer in practical ZABs[15-18].

In the mass transfer optimization of air cathode catalysts for ZABs, the construction of porous architectures has been demonstrated as an effective strategy to optimize oxygen diffusion pathways and enhance active site exposure[19-21]. Moreover, recent studies demonstrate that the concave curvature of porous channels can optimize the adsorption strength of key intermediates by inducing electronic structure distortion at active sites, thereby significantly enhancing the ORR kinetics[22]. Current pore-engineering strategies primarily include: hard templating techniques (e.g., ZnO/SiO_2 sacrificial templates), etching approaches (e.g., KOH or plasma etching), and high-temperature pyrolysis-induced phase separation mechanisms[23,24]. For instance, Song *et al.* prepared FeCo/NC with 3D ordered hierarchical porous structure using a hard template [polystyrene (PS) microsphere] and inhomogeneous nucleation[25]. The unique 3D ordered hierarchical porous structure significantly optimizes the mass transfer kinetic pathway. Zhang *et al.* successfully constructed hierarchical pore systems through the pyrolysis of metal-organic framework (MOF) precursors, providing efficient mass transfer pathways for electrocatalytic CO_2 reduction[26]. Recently, two-dimensional (2D) nanomaterials have become an attractive choice for pore engineering due to their high surface-to-volume ratio, which provides densely populated active sites per unit mass, and their atomic-scale thickness, which significantly reduces mass transfer resistance[27-29]. However, significant technical challenges arise when implementing these pore-engineering strategies in 2D material systems. Frequently, template removal and etching processes induce in-plane fractures or stacking collapse of the 2D layered structures, thereby reducing electrical conductivity and structural stability[30,31]. In addition, due to the relatively high surface energy of 2D materials, they are prone to structural collapse or agglomeration during high-temperature pyrolysis, compromising the stability of the pore structure[32-34]. In contrast, the micelle interface self-assembly method forms dynamically ordered templates via amphiphilic molecule self-assembly on 2D surfaces. This process relies on weak intermolecular interactions, avoiding the mechanical stress and chemical corrosion inherent in etching or template removal[35,36]. Moreover, the micellar layer on the surface effectively mitigates thermal stress during high-temperature calcination, preventing structural collapse or agglomeration[37]. Therefore, this approach ensures the construction of efficient mass transfer channels while preserving material structural integrity.

Herein, we constructed an interconnected hierarchical porous structure with mesopores and micropores in 2D Fe/N-codoped carbon nanoleaves (Meso/Micro-FeNC). The mesopores on the surface were directed by F127/1,3,5-trimethylbenzene (TMB) micelles, while the micropores originated from 2D Fe-doped Zeolitic Imidazolate Framework-L (ZIF-L) precursors, resulting in an interconnected hierarchical porous architecture. The as-prepared Meso/Micro-FeNC features interconnected porous channels, a high surface area, and accessible $Fe-N_x$ active sites. These characteristics improve mass transfer and provide more accessible active sites. Meanwhile, 2D hollow structure ensures mechanical robustness. Assembled ZABs delivered an open-circuit potential of 1.52 V with a remarkable specific capacity of 787.6 mAh g^{-1} at 20 mA cm^{-2}, higher than those of Pt/C (1.48 V, 673.9 mAh g^{-1}). Kinetic experiments confirm that Meso/Micro-FeNC enables rapid mass transfer. Density functional theory (DFT) calculations confirm that FeN_x sites with concave curvature can weaken the over-absorption of $^*OH$, thus facilitating the ORR. This work presents a novel approach for optimizing mass transfer in ZAB catalysts for air electrode through the construction of interconnected hierarchical pore structures at 2D interfaces.

EXPERIMENTAL

Synthesis of ZIF-L-Fe and ZIF-L

First, 0.594 g of $Zn(NO_3)_2$ and 5.2 mg of ferric ammonium citrate were dissolved in 40 mL of H_2O to prepare Solution A. Separately, 1.314 g of 2-methylimidazole was dissolved in 40 mL of H_2O to prepare Solution B. Subsequently, Solution B was rapidly poured into Solution A and stirred for 4 h at room temperature. The mixture was washed three times with ethanol and centrifuged at 8000 rpm for 5 min to obtain yellow ZIF-L-Fe. The product was then dried in an oven at 60 °C for future use.

For the synthesis of ZIF-L, the same procedure was followed, omitting the addition of ferric ammonium citrate, ultimately yielding white ZIF-L product.

Synthesis of ZIF-L-Fe@F127 micelle

First, 0.1 g of F127 and 20 mg of dopamine (DA) were dissolved in a mixed solution of 5 mL H_2O and 5 mL ethanol. The mixture was stirred slowly at 500 rpm for 30 min at room temperature. Then, 2 mL of TMB was added to form a microemulsion system, and stirring was continued at room temperature for 3 h until the system was stabilized. Subsequently, 100 mg of pre-synthesized ZIF-L-Fe was dispersed in a mixed solution of 10 mL H_2O and 10 mL ethanol. This dispersion was gradually added into the previously prepared microemulsion system. The pH of the solution was adjusted to 8.5 using Tris-HCl buffer solution, and stirring was continued at 500 rpm for 48 h at room temperature. Finally, the mixture was centrifuged at 8000 rpm for 5 min and washed three times with ethanol and H_2O to obtain ZIF-L-Fe@F127. The product was then dried in an oven at 60 °C for future use.

Synthesis of Meso/Micro-FeNC, FeNC, NC

ZIF-L-Fe@F127 micelle, ZIF-L-Fe, and ZIF-L samples were separately loaded into a tube furnace. The samples were heated at a rate of 2 °C min^{-1} to 350 °C and maintained at this temperature for 2 h under an Ar atmosphere. The temperature was elevated to 900 °C at the same rate and held for an additional 2 h. After cooling to room temperature, Meso/Micro-FeNC, Fe-NC, and NC were obtained.

RESULTS AND DISCUSSION

Figure 1A illustrates the synthesis of Meso/Micro-FeNC, which features single-atom Fe dispersed on interconnected hierarchical porous hollow nanoleaves. Typically, ZIF-L-Fe is pre-synthesized via a coordination-driven self-assembly strategy. This involves mixing aqueous solutions of 2-mim with zinc salts, and iron salts to construct the framework through metal-ligand coordination. For the iron source, we

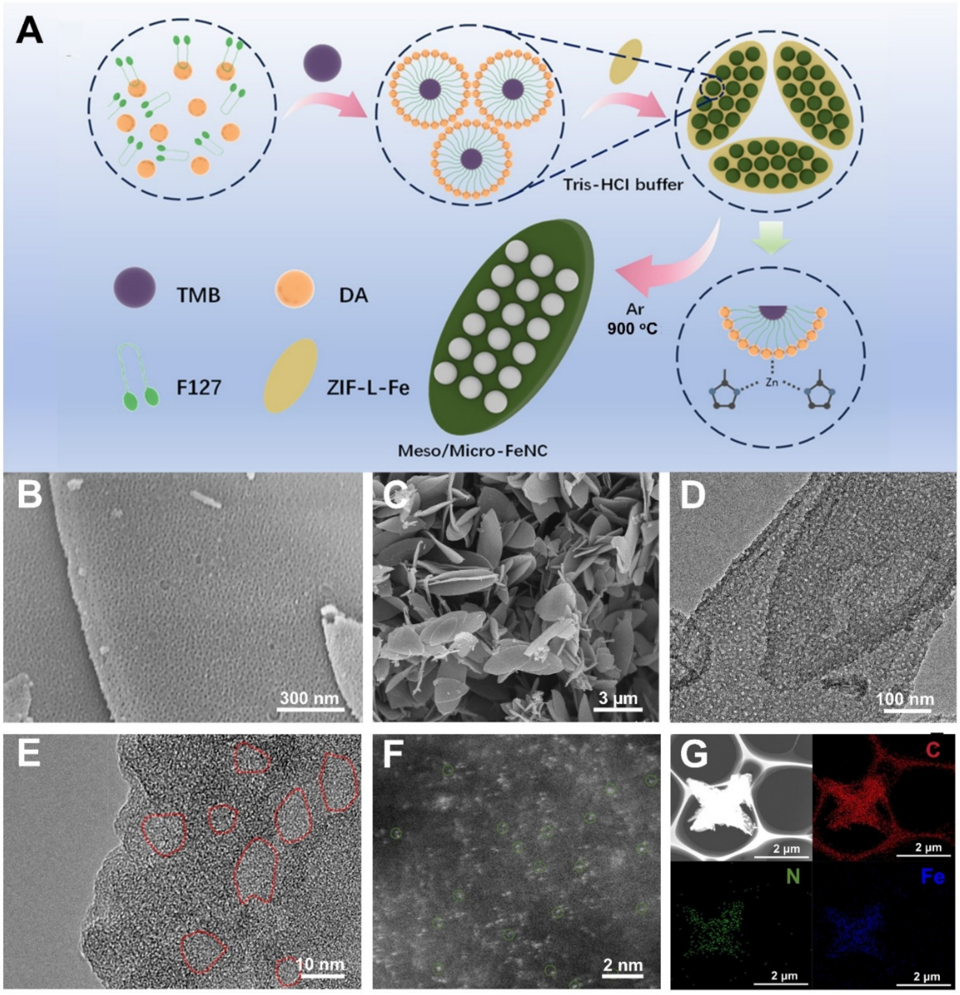

Figure 1. (A) The preparation process of Meso/Micro-FeNC; (B) SEM image of ZIF-L-Fe@micelle; (C) SEM and (D) TEM image of Meso/Micro-FeNC; (E) High resolution TEM image of Meso/Micro-FeNC (red circles: mesopores); (F) Aberration-corrected HAADF-STEM image of Meso/Micro-FeNC; (G) EDX elemental mapping of Meso/Micro-FeNC. Meso/Micro-FeNC: Meso/microporous Fe/N-codoped carbon; SEM: scanning electron microscopy; ZIF-L: zeolitic imidazolate framework-L; TEM: transmission electron microscopy; HAADF-STEM: high-angle annular dark-field scanning transmission electron microscopy; EDX: energy-dispersive X-ray spectroscopy.

preferentially select ferric ammonium citrate, because the carbonyl group (C=O) in citrate anions can form strong coordination with Zn in the ZIF-L framework, partially replacing the original 2-mim ligands. This ligand exchange maintains the structural integrity of the ZIF crystals while establishing a Fe-Zn mixed coordination environment[38]. This environment facilitates Zn evaporation and the formation of Fe-N_x active sites during pyrolysis, without destroying the leaf-like architecture. Furthermore, active nitrogen species generated from the decomposition of ammonium ions during pyrolysis synergistically promote the formation of atomically dispersed Fe-N_x active sites. Compared to inorganic iron salts (e.g., $FeCl_3$), ferric ammonium citrate offers superior aqueous solubility, which prevents active site aggregation or framework defects caused by hydrolysis-induced precipitation, while eliminating risks associated with residual corrosive anions. Subsequently, Pluronic F127, DA, and TMB are combined to assemble a DA layer on the surface of pre-synthesized ZIF-L-Fe (ZIF-L-Fe@micelle) via a nanoemulsion assembly strategy. Subsequently, a segmented pyrolysis protocol is applied. Initially, the surfactant is removed at a relatively low temperature, followed by high-temperature graphitization of the precursor. This two-step pyrolysis strategy effectively preserves the integrity of the pore structure, leading to the successful synthesis of Meso/Micro-FeNC. For comparison, Fe/NC without a hierarchical porous structure was synthesized without surfactant micelles, while NC without Fe single-atom dispersion or a hierarchical porous structure was synthesized by omitting the iron source and surfactant micelles.

As shown in the field-emission scanning electron microscopy (SEM) images in Figure 1B, the successful synthesis of the ZIF-L-Fe@micelle precursor is demonstrated, with ordered mesopores observed on its surface. After high-temperature pyrolysis process, the resulting Meso/Micro-FeNC retains the 2D leaf-like morphology of the precursor MOF [Figure 1C]. Transmission electron microscopy (TEM) image reveals a roughened surface composed of a continuous honeycomb-like mesoporous network and hollow cavities, with no metal nanoparticles [Figure 1D]. This hierarchical architecture provides more accessible active sites and enhances electrocatalytic mass transfer processes. High-resolution TEM image shows no iron nanoparticles or lattice fringes, confirming the high dispersion of iron species [Figure 1E]. Additionally, mesoporous structures with a pore size of approximately 6 nm (marked in red circles) were observed. Further insights into the atomic configuration of active sites were conducted using aberration-corrected high-angle annular dark-field scanning transmission electron microscopy (HAADF-STEM). The aberration-corrected HAADF-STEM image [Figure 1F] further reveals a high density of discrete bright spots (highlighted by green circles), directly demonstrating atomic-level Fe dispersion. Energy-dispersive X-ray spectroscopy (EDX) elemental mapping [Figure 1G] demonstrates the uniform distribution of C, N, and Fe within the 2D leaf-like framework, indicating the successful conversion of the iron precursor into high-density Fe-N_x active sites during pyrolysis. This feature is important for maximizing atomic utilization efficiency. For comparison, Fe-NC (derived from ZIF-L-Fe) and NC (from ZIF-L) were characterized by SEM [Supplementary Figures 1 and 2]. While Fe-NC maintains the distinctive 2D morphology, NC collapses and agglomerates due to the inherent instability of 2D ZIF-L structure. During high-temperature pyrolysis, volatilization of Zn species disrupts the leaf-like morphology. However, the incorporation of Fe^{3+} stabilizes the 2D structure by forming stronger coordination bonds with organic ligands, preserving the 2D framework without altering the coordination mode. Notably, unlike Meso/Micro-FeNC, Fe-NC lacks a continuous mesoporous network, with Fe nanoparticles forming on the Fe-NC [Supplementary Figure 3]. This structural distinction is expected to significantly influence their catalytic activities.

The structural properties of Meso/Micro-FeNC, Fe-NC, and NC were analyzed in depth using powder X-ray diffraction (XRD). The three ZIF-L precursors showed profiles similar to those of the simulated ZIF-L crystals, indicating that the introduction of Fe species and surfactant micelles does not influence the crystalline structure of ZIF-L [Supplementary Figure 4]. The powder XRD patterns of all three catalysts showed a broad diffraction peak around 20°-30° [Supplementary Figure 5], which corresponded to the (002) crystalline plane of graphitic carbon[39]. Notably, no diffraction peaks related to Fe species were observed in Meso/Micro-FeNC, indicating the atomically dispersed state of Fe species, consistent with characterization results obtained by TEM. In contrast, the Fe-NC sample exhibits a weak diffraction peak at $2\theta \approx 45°$ that matches the (110) plane of metallic Fe (PDF#06-0696), suggesting potential formation of Fe nanoparticles. This conclusion is corroborated by Fe nanoparticles observed in TEM images. Furthermore, the defect structures of the Meso/Micro-FeNC and Fe-NC were characterized using Raman spectroscopy. The Raman spectra [Supplementary Figure 6] showed two main peaks at 1,350 cm^{-1} and 1,580 cm^{-1}, assigned to the defective carbon (D-band, defective carbon) and graphitic carbon (G-band, graphitic carbon)[40]. The I_D/I_G ratio of Meso/Micro-FeNC (1.06) is higher than 0.98 for Fe-NC, suggesting a greater degree of defects in Meso/Micro-FeNC. These defects likely arise from the coordination between polydopamine and Fe^{3+} in the precursor ZIF-L, as well as the high-temperature decomposition of organic ligands[41]. As shown in N_2 adsorption/desorption isotherms [Figure 2A], Brunauer-Emmett-Teller (BET) specific surface area of Meso/

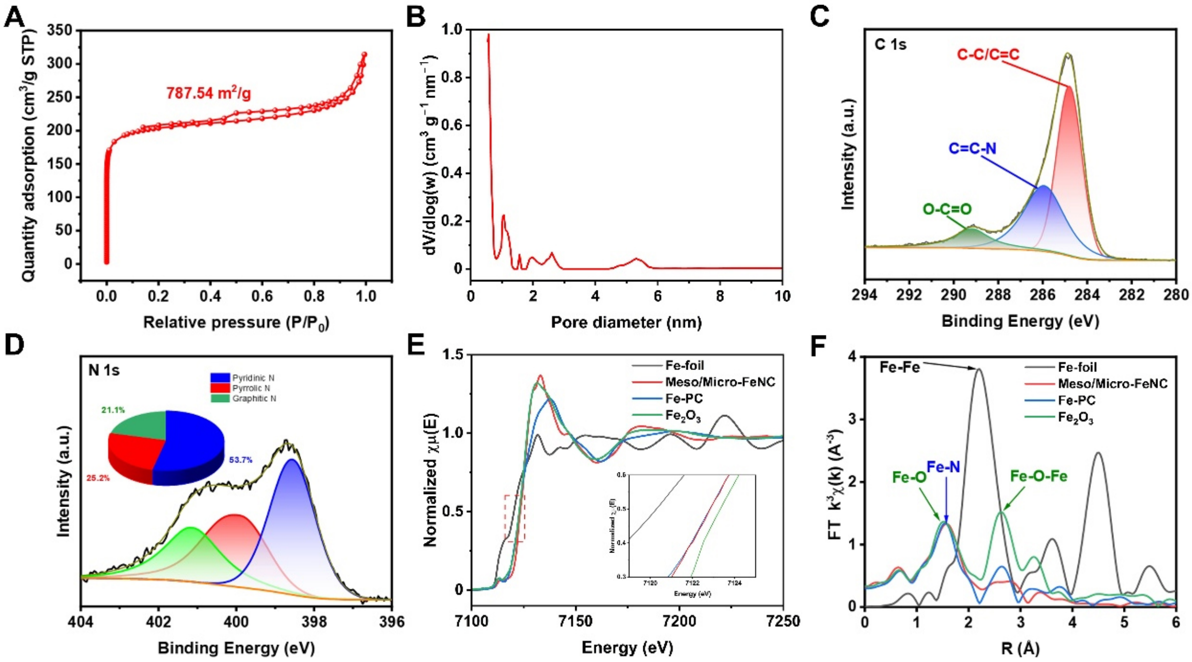

Figure 2. (A) N_2 adsorption/desorption isotherms and (B) pore size distribution of Meso/Micro-FeNC; (C) XPS high-resolution spectra of C 1s and (D) N 1s for Meso/Micro-FeNC; (E) Fe K-edge XANES spectra and (F) FT k^3-weighted EXAFS spectra of Fe foil, Meso/Micro-FeNC, FePc, and Fe_2O_3. Meso/Micro-FeNC: Meso/microporous Fe/N-codoped carbon; XPS: X-ray photoelectron spectroscopy; XANES: X-ray absorption near-edge structure.

Micro-FeNC was 787.5 m^2 g^{-1}. A microporous filling effect was observed in the region of $P/P_0 < 0.1$, which proved the presence of micropores. Furthermore, the material showed a Type IV hysteresis loop, suggesting the mesoporous structure exists in the material[42]. The pore size distribution revealed that the mesopores were mainly concentrated at 2.5 nm and 5.2 nm [Figure 2B], which was consistent with the High-resolution TEM results. For comparison, Fe-NC showed a lower BET surface area (690.8 m^2 g^{-1}) [Supplementary Figure 7], with pore size distribution showing predominantly micropores [Supplementary Figure 8]. The microporous volume and mesoporous volume of the Meso/Micro-FeNC material are 0.26 cm^3 g^{-1} and 0.22 cm^3 g^{-1}, respectively [Supplementary Table 1]. The calculated mesoporous/microporous volume ratio of Meso/Micro-FeNC is 0.84, which is superior to that of Fe-NC (0.60). For Meso/Micro-FeNC, the enhanced BET surface area provides abundant exposed active sites for electrochemical reactions, while the mesopores facilitate efficient mass transport of electrolytes and intermediates to catalytic sites.

The chemical states of the elements in Meso/Micro-FeNC and Fe-NC were further analyzed by X-ray photoelectron spectroscopy (XPS) [Supplementary Figure 9]. The results indicate that C, N, and O are present in the spectra of both Meso/Micro-FeNC and Fe-NC. As predicted, the Fe element is not detected in the survey scan spectra due to its relatively low content. The C 1s high-resolution spectrum shows three peaks assigned to O-C=O at 289.2 eV, C=C-N at 286.0 eV, and C=C/C-C at 284.8 eV [Figure 2C]. The N 1s high-resolution spectrum indicates three N forms in Meso/Micro-FeNC pyrrolic-N at 398.6 eV, pyridinic-N at 400.1 eV, and graphitic-N at 401.2 eV [Figure 2D][43]. These results confirm the high density of N sites in Meso/Miro-FeNC, which can effectively anchor Fe species. The Fe 2p spectrum exhibits two pairs of double peaks, which correspond to Fe^{2+} (724.7 eV and 710.9 eV) and Fe^{3+} (728.1 eV and 714.9 eV), along with two satellite peaks [Supplementary Figure 10][44,45]. No peaks associated with Fe^0 or other Fe compounds are observed, consistent with the XRD and TEM results. The chemical states of C, N, and Fe in Fe-NC are similar to those in Meso/Micro-FeNC [Supplementary Figures 11-13]. Notably, although Fe-NC and

Meso/Micro-FeNC have the same chemical composition, their structural differences suggest that the variation in their ORR performance arises primarily from their distinctive pore structures, which play a crucial role in determining the catalytic activity.

The coordination environment and atomic dispersion of Fe species in Meso/Micro-FeNC were further investigated using X-ray absorption near-edge structure (XANES) and extended X-ray absorption fine structure (EXAFS). The near-edge energy adsorption threshold lies between Fe_2O_3 and iron phthalocyanine (FePc), but closer to FePc [Figure 2E]. This indicates an iron valence state intermediate between +2 and +3, with a stronger tendency toward +2. The XANES spectra of both Meso/Micro-FeNC and FePc exhibit a peak at 7,112 eV, characteristic of the square plane of $Fe\text{-}N_4$ coordination. The Fourier transform to the R-space exhibits a dominant peak at 1.56 Å, with no detectable Fe-Fe or Fe-O-Fe bonding [Figure 2F], confirming that Fe is dispersed as atomically dispersed sites in Meso/Micro-FeNC[46-48]. Further supporting evidence comes from the wavelet transform (WT) analysis, which clearly demonstrates the presence of Fe-N coordination in Meso/Micro-FeNC [Supplementary Figure 14][49]. These results confirm that the Fe-N coordination structure was successfully anchored in the catalyst. To further clarify the metal content in the materials, thermogravimetric (TG) analysis was conducted on Meso/Micro-FeNC and Fe-NC [Supplementary Figure 15]. The results indicate that Fe content is calculated to be 3.50 wt% for Meso/Micro-FeNC and 6.64 wt% for Fe-NC. The slight difference is attributed to the protective effect of surface micelles during pyrolysis. Specifically, the micellar framework in Meso/Micro-FeNC acts as a physical barrier to suppress Fe thermal migration, maintaining atomic dispersion. In contrast, the absence of such protection in Fe-NC facilitates Fe thermal migration at high temperatures, leading to loss of N-doped carbon framework and high Fe content. This structural evolution highlights the crucial role of micellar templating in regulating metal dispersion and loading during synthesis. Notably, although Meso/Micro-FeNC shows a slightly lower Fe loading compared to Fe-NC, its ORR performance is superior due to the enhanced accessibility and uniform distribution of active sites rather than merely total metal content. The atomic dispersion in Meso/Micro-FeNC ensures optimal utilization of each Fe active center, improving catalytic efficiency.

The ORR performance of Meso/Micro-FeNC was evaluated using a rotating disk electrode (RDE) in 0.1 M KOH, with an obvious reduction peak of Meso/Micro-FeNC at 0.74 V under O_2-saturated conditions, while no peak was observed under Ar-saturated conditions [Figure 3A], indicating that Meso/Micro-FeNC shows oxygen reduction activity. Linear scanning voltammetry (LSV) revealed that Meso/Micro-FeNC possessed a half-wave potential ($E_{1/2}$) of 880 mV, outperforming both Fe-NC (830 mV) and commercial 20% Pt/C (860 mV) [Figure 3B]. As demonstrated in Figure 3C, the Tafel slopes of the three materials are 82 mV dec^{-1} for Meso/Micro-FeNC, 94 mV dec^{-1} for Fe-NC, and 112 mV dec^{-1} for Pt/C. This suggests that the Meso/Micro-FeNC has faster ORR kinetics. Electrochemical impedance spectroscopy (EIS) analysis further supports these findings. As evidenced by the Nyquist curves and fitting results in Supplementary Figure 16, along with the kinetic parameters [Supplementary Table 2]. Meso/Micro-FeNC exhibits superior charge transfer kinetics compared to Fe-NC. The charge transfer resistance (Rct = 34.91 Ω) of is significantly lower than that of Fe-NC (55.45 Ω). The Warburg coefficient (W1-R, reflecting the mass transfer kinetic characteristics) for Meso/Micro-FeNC is 16.57 Ω, which is also lower than the 43.95 Ω for Fe-NC. These results confirm that Meso/Micro-FeNC possesses a smaller impedance arc radius, indicating reduced charge transfer resistance and optimized mass transport, thus enabling more efficient charge and mass transfer. This phenomenon is consistent with the electrochemical kinetic advantages expected from the material structure design. The surface-ordered mesopores play a crucial role in improving ORR activity. To analyze the intrinsic activity, we determined the electrochemically active surface area (ECSA) via C_{dl} measurement [Supplementary Figure 17]. Meso/Micro-FeNC exhibits a higher C_{dl} (8.4 mF cm^{-2}) than Fe-NC

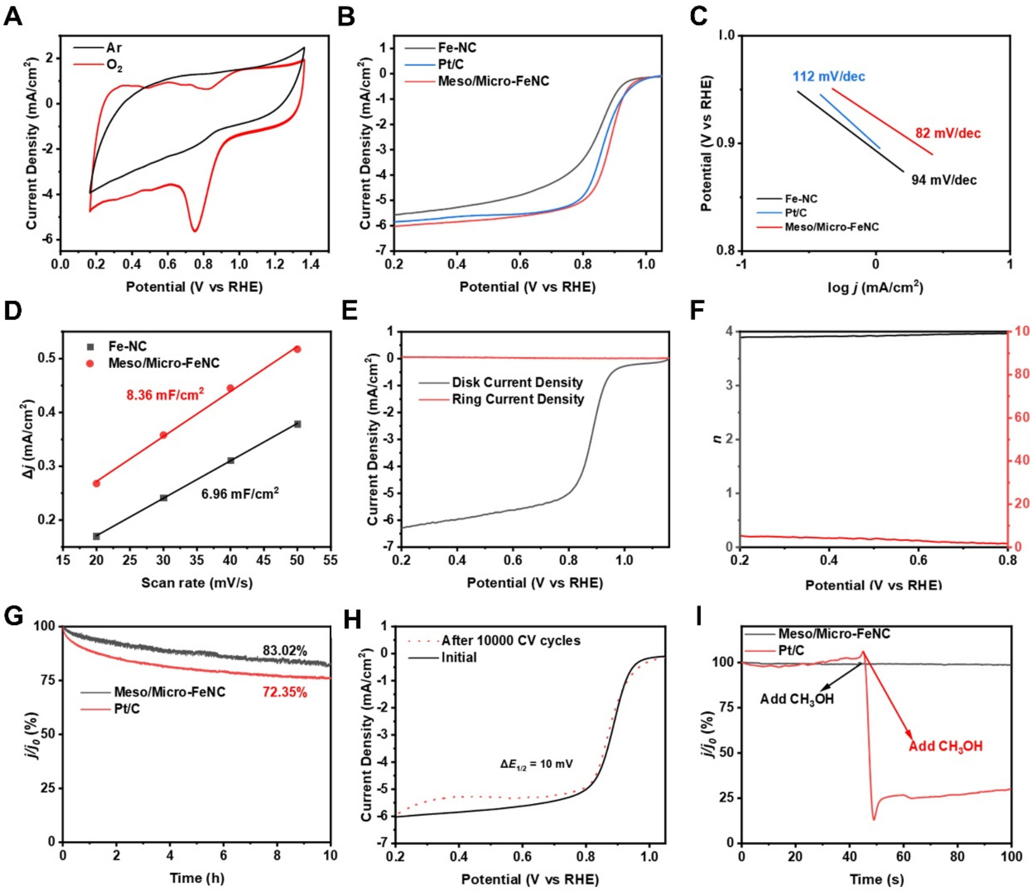

Figure 3. (A) CV curves of Meso/Micro-FeNC under O_2/Ar saturation, (B) LSV curves of Meso/Micro-FeNC, Fe-NC and Pt/C catalysts under O_2 saturation and 1600 rpm and (C) Tafel slopes of Meso/Micro-FeNC, Fe-NC, and Pt/C catalysts; (D) The C_{dl} value of Fe-NC and Meso/Micro-FeNC, (E) LSV curves of Meso/Micro-FeNC using RRDE under 1600 rpm and (F) electron transfer number and the yield of H_2O_2 at different potentials; (G) *j-t* curves for the catalysts Meso/Micro-FeNC and Pt/C, (H) LSV curves of Meso/Micro-FeNC before and after 10000 cycles of CV test and (I) methanol tolerance experiments on Meso/Micro-FeNC and Pt/C. CV: Cyclic voltammetry; Meso/Micro-FeNC: meso/microporous Fe/N-codoped carbon; LSV: linear scanning voltammetry; RRDE: rotating ring-disk electrode.

(7.0 mF cm^{-2}) [Figure 3D]. Subsequently, the ECSA of Meso/Micro-FeNC was 522.5 m^2 g^{-1}, which is higher than that of Fe-NC (435.0 m^2 g^{-1}) [Supplementary Figure 18]. The high ECSA value of Meso/Micro-FeNC suggests that more active sites are exposed. These additional active sites further generate a richer three-phase interface, which significantly improves the utilization efficiency of the active sites and establishes a robust foundation for high-efficiency ORR catalysis.

To elucidate the ORR reaction pathway of Meso/Micro-FeNC, the number of transferred electrons of Meso/Micro-FeNC was tested using rotating ring-disk electrode (RRDE). The calculated transferred electrons number (n) from LSV curves was ≈ 4, while the yield of hydrogen peroxide was less than 10% [Figure 3E and F]. RDE measurements were performed at 400-2500 rpm [Supplementary Figure 19A]. The limiting current density of Meso/Micro-FeNC increases with the increase of rotation speed. Furthermore, a good linear correlation between j^{-1} and $\omega^{-1/2}$ was observed, consistent with the mass transfer behavior described by the K-L equation [Supplementary Figure 19B]. The fitting analysis yielded an electron transfer number (n) of ~3.8, in agreement with the RRDE results. The results demonstrate that Meso/Micro-FeNC shows high $4e^-$ selectivity in alkaline media, with O_2 reducing to H_2O during electrocatalysis. The excellent

$4e^-$ selectivity benefits from the high surface site density (SD) of Fe-N_x in Meso/Micro-FeNC[50].

In order to investigate the stability of Meso/Micro-FeNC, the ORR durability tests were conducted in O_2-saturated 0.1 M KOH solution under different conditions. After a 10-h electrolysis process, Meso/Micro-FeNC maintained 83.0% of a high initial current density, which was significantly higher than the 72.3% observed for commercial Pt/C [Figure 3G]. After cycling 10000 cyclic voltammetry (CV) cycles at 1600 rpm, the $E_{1/2}$ of Meso/Micro-FeNC value decreased by only 10 mV [Figure 3H], further confirming its robust performance stability. To evaluate the structural stability during electrocatalysis, we characterized the post-electrolysis materials. As evidenced in Supplementary Figure 20, the leaf-like morphology of Meso/Micro-FeNC remained without observable collapse or aggregation after stability test. Moreover, no characteristic diffraction peaks corresponding to Fe-based species were detected in XRD pattern, confirming the absence of Fe nanoparticle formation [Supplementary Figure 21]. The results demonstrate that the Fe-N_x active sites remained stable during electrocatalysis, with no significant metal leaching, migration, or agglomeration. These findings confirm the exceptional electrochemical stability of the Meso/Micro-FeNC catalyst. Methanol tolerance was also carried out by adding 1 mL of methanol during the process of electrolysis. As shown in Figure 3I, the Meso/Micro-FeNC remained relatively constant before and after the addition of methanol, whereas the current density of the Pt/C decreased significantly following the addition of methanol. These results demonstrate the remarkable stability of Meso/Micro-FeNC and outstanding methanol tolerance during ORR. These advantages make the electrocatalyst a promising candidate for practical applications.

ZABs were assembled using Meso/Micro-FeNC catalysts on air electrode and Zn foils as the other electrode, with Pt/C+Ir/C as a benchmark [Figure 4A]. To ensure OER activity, Ir/C was added into air cathode. At a current density of 20 mA cm^{-2}, the discharge specific capacity of Meso/Micro-FeNC+Ir/C was 787.6 mAh g^{-1}, which was better than that of the Pt/C+Ir/C catalyst (673.9 mAh g^{-1}) [Figure 4B]. The Meso/Micro-FeNC+Ir/C based ZABs demonstrated an open-circuit voltage of 1.52 V, which is higher than that of the Pt/C+Ir/C-assembled battery (1.48 V), indicating its superior intrinsic ORR kinetics [Figure 4C]. The discharge polarization curves reveal that the Meso/Micro-FeNC+Ir/C based ZABs exhibit a higher discharge plateau and a peak power density of 178.4 mW cm^{-2}, exceeding that of the Pt/C+Ir/C catalyst (146.7 mW cm^{-2}) [Figure 4D]. Long-term charge/discharge cycling tests demonstrate that the Meso/Micro-FeNC+Ir/C-based ZABs maintain stable charge/discharge cycling for over 160 h, with a voltage gap of 790 mV (5 mA cm^{-2}), significantly lower than Pt/C+Ir/C (950 mV) [Figure 4E]. Post-cycling discharge curves at varied current densities confirmed retained ORR activity and reversibility [Supplementary Figure 22]. Additionally, we compared the ORR and ZAB performance of the Meso/Micro-FeNC with those of similar electrocatalysts reported in relevant literature. As shown in Supplementary Table 3, Meso/Micro-FeNC demonstrates remarkable advantages in both ORR and ZAB performance, with its comprehensive performance superior to most similar electrocatalysts. The above results collectively underscore the potential of Meso/Micro-FeNC for advanced energy conversion and storage technologies.

In-situ EIS coupled with distribution of relaxation time (DRT) analysis was applied to investigate the Meso/Micro-FeNC catalyst at various state-of-charge (SOC) and state-of-discharge (SOD) potentials. This approach enables decoupling of electrode kinetic behaviors from the EIS spectra, enabling elucidation of the mass transport kinetics of the ZAB system under realistic operational conditions[51-53]. As illustrated in Figure 5A and B, *in-situ* EIS measurements were conducted across the electrochemical window, covering the charging polarization region (~1.8 V) and discharging stabilization region (~1.3 V). The EIS spectra reveal that the interfacial kinetics of the ZABs are dominated by low-frequency (LF) characteristics (1~10 s), exhibiting distinct Warburg impedance features associated with O_2/OH^- diffusion and intermediate species

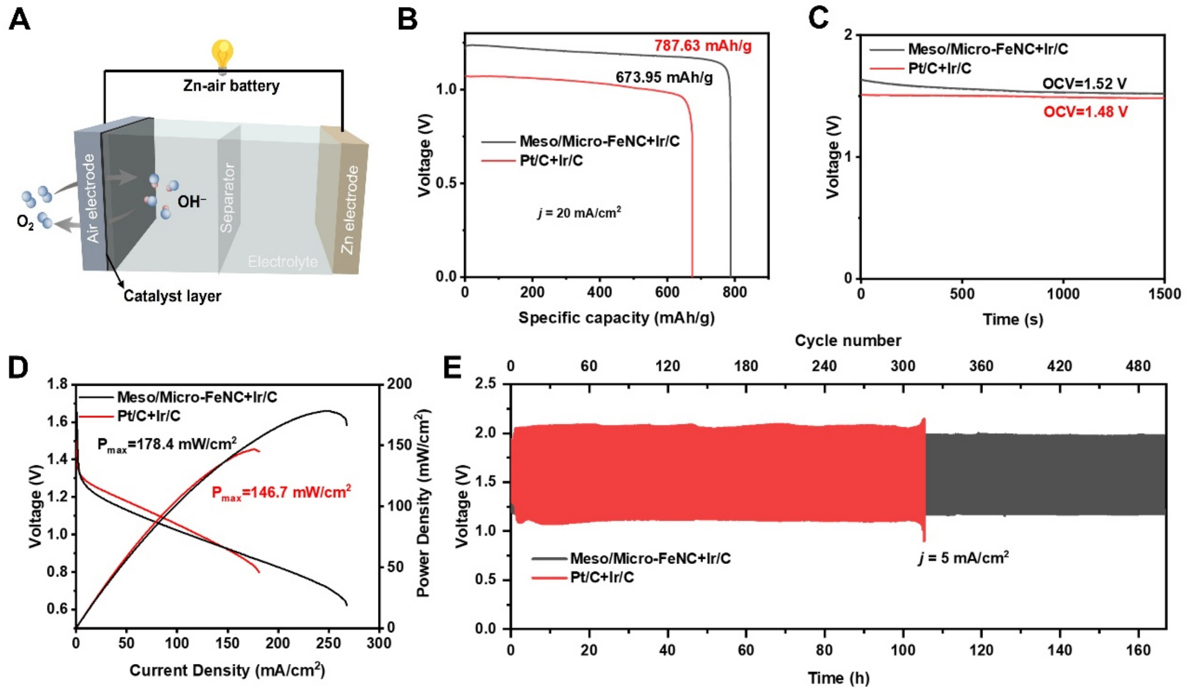

Figure 4. (A) Electrochemical performances of ZABs assembled with catalysts. Schematic diagram of a ZAB; (B) Discharge specific capacity curves at current density of 20 mA cm^{-2}, (C) open-circuit voltages, (D) discharge polarization curves, and the power densities of Meso/Micro-FeNC+Ir/C and Pt/C+Ir/C; (E) Galvanostatic long-term charge and discharge profiles of Meso/Micro-FeNC+Ir/C and Pt/C+Ir/C. ZABs: Zinc-air batteries; Meso/Micro-FeNC: meso/microporous Fe/N-codoped carbon.

transport during the charging of OER and discharging of ORR[54]. In contrast, the intermediate-frequency (IF) charge transfer resistance (electron transfer at Fe-N$_4$ sites) contributes only 7%~15% to the total impedance, while LF impedance components account for over 85% [Figure 5C]. The dominance of this LF response demonstrates that mass transport at the three-phase interface (O$_2$ diffusion, electrolyte permeation, and intermediate accumulation) plays an important role in determining electrode performance under operational conditions[55-57]. As shown in Supplementary Figure 23, conventional Fe-NC exhibits a larger LF peak area than Meso/Micro-FeNC, indicating stronger mass transport limitations due to its micropore-dominated structure (consistent with BET results)[58,59]. We attribute this diffusion resistance primarily to hindered O$_2$/intermediate transport within its micropore-dominated structure. The left-shift and reduction of the LF peak during charge processes reflect enhanced mass transfer [Figure 5C]. Furthermore, the IF peak representing charge transfer also exhibits a left-shift, indicating that charge transfer accelerates along with enhanced mass transport [Figure 5D]. During the discharge process [Figure 5E and F], the coordinated evolution of the LF and IF peaks collectively suggests optimization of mass transport. These results establish a clear structure-activity relationship between the hierarchical pore architecture of Meso/Micro-FeNC and its mass transport-dominated interfacial kinetics.

To gain deeper insight into the effect of substrate negative curvature on catalytic activity, we performed DFT calculations of the ORR mechanisms on FeN$_4$ sites supported on both planar and curved graphene. To construct a smooth concave surface, we employed a hydrogen-saturated half-carbon nanotube (CNT) model derived from a (12,0) CNT (radius = 4.88 Å, curvature = 0.20 Å^{-1}), as detailed in the Computational methods section. Figure 6 presents the free energy diagrams for the ORR on planar and curved catalysts at a potential of U = 0.46 V, corresponding to the equilibrium potential at pH = 13. For the negatively curved Fe-N-C system, the potential-determining step (PDS) occurs at the third proton-coupled electron transfer

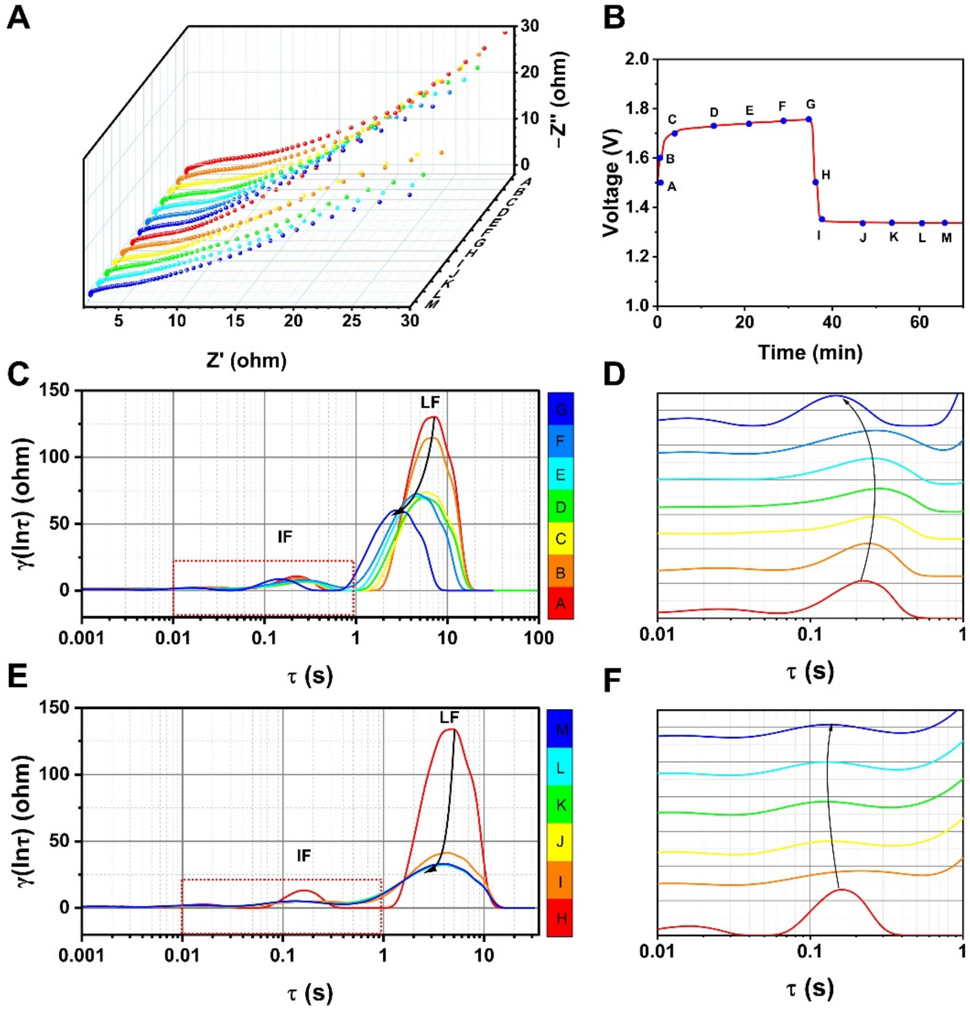

Figure 5. Electrochemical analysis of Meso/Micro-FeNC and FeNC. (A) *In-situ* EIS of Meso/Micro-FeNC at different charge-discharge potentials in a ZAB; (B) The corresponding test potentials for *in-situ* EIS on the initial charge-discharge curves of the ZAB; (C) DRT plot of Meso/Micro-FeNC obtained by deconvolving the *in-situ* EIS during charge processes; (D) The enlarged view of the IF peak of the charge DRT; (E) DRT plot of Meso/Micro-FeNC obtained by deconvolving the *in-situ* EIS during discharge processes; (F) The enlarged view of the IF peak of the discharge DRT. Meso/Micro-FeNC: Meso/microporous Fe/N-codoped carbon; ZABs: zinc-air batteries; EIS: electrochemical impedance spectroscopy; DRT: distribution of relaxation time; IF: intermediate-frequency.

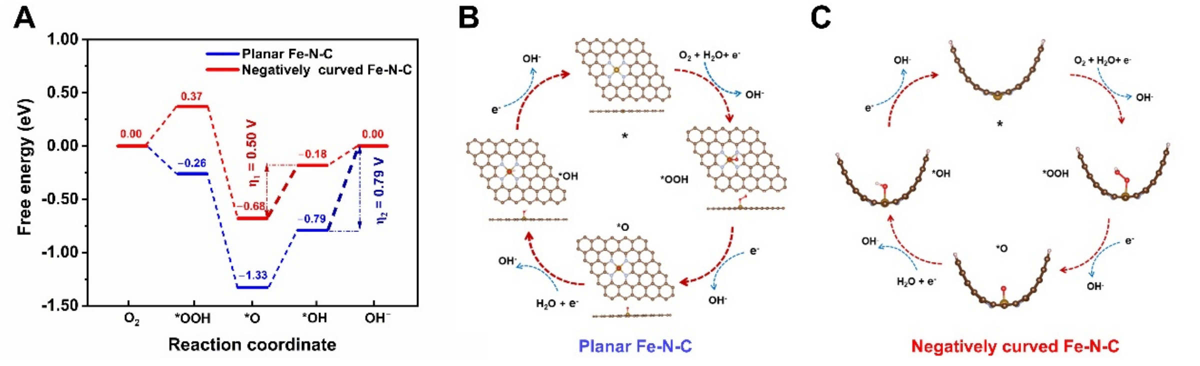

Figure 6. (A) Free energy profiles and catalytic cycles of ORR on (B) planar and (C) negatively curved Fe-N-C catalysts at U = 0.46 V. ORR: oxygen reduction reaction.

(PCET) step (*O → *OH), with an overpotential (η) of 0.50 V. In contrast, the planar Fe-N-C catalyst exhibits a PDS at the final PCET step (*OH → OH^-), with a calculated overpotential of 0.79 V. The enhanced ORR activity observed on the concave surface is attributed to the moderate weakening of *OH intermediate adsorption, as evidenced by the shift in the PDS and the reduction in η. This finding is consistent with previous reports that the inner walls of CNTs can promote ORR activity[60]. The origin of this behavior lies in the structural deformation imposed by the concave surface and the reduced orbital interactions, which together lower the *OH binding energy, thereby facilitating the ORR activity.

CONCLUSIONS

In conclusion, we prepared a single-atom Fe-NC hollow nano-leaf ORR catalyst with microporous and mesoporous structures (Meso/Micro-FeNC) using nano-emulsion-induced self-assembly. Experimental results demonstrate that the structural evolution of the surface coating into hierarchical pores is crucial for improving mass transfer and providing more accessible active sites and. Meso/Micro-FeNC exhibits a high ECSA of 522.5 $m^2 g^{-1}$ and a high density of Fe-N active sites. Benefiting from these advantages, Meso/Micro-FeNC demonstrates exceptional ORR performance, including an $E_{1/2}$ of 880 mV, excellent $4e^-$ pathway selectivity, and remarkable methanol tolerance. Furthermore, ZABs utilizing Meso/Micro-FeNC as the electrode exhibit a peak power density of 178.4 mW cm^{-2} and outstanding galvanostatic discharge performance, highlighting their superior activity and stability in practical applications compared to Pt/C. In addition, *in-situ* EIS measurements reveal distinct characteristics of Meso/Micro-FeNC and Fe-NC in mass transport behavior, validating the optimization of the hierarchical pore structure for mass transport-dominated interfacial kinetics. DFT calculations demonstrate that the Fe-N_x active sites with concave curvature can effectively lower the adsorption energy of *OH. Therefore, this hierarchical pore architecture not only accelerates mass transport but also changes the PDS to reduce η, thereby synergistically enhancing the ORR performance. This work expands the carriers for the preparation of highly efficient ORR single-atom catalysts by micellar self-assembly strategy, significantly advancing the design of advanced catalysts for energy applications.

DECLARATIONS

Authors' contributions

Data curation, formal analysis, investigation, methodology, software, validation, writing - original draft: Song, L.; Liu, Y.
Investigation, data curation, software: Wang, J. J.; Wu, R.
Correcting and conceptualization, formal analysis and supervision: Zhang, H.; Dang, J. S.; Zhang, W.; Cao, R.
Visualization, formal analysis, writing-review & editing, conceptualization, funding acquisition: Zheng, H.

Availability of data and materials

Morphology and structure for the material characterizations and the electrochemical performance of materials for exploration and comparison are presented in the Supplementary Materials. Further data are available from the corresponding author upon reasonable request.

Financial support and sponsorship

We gratefully acknowledge the financial support from National Natural Science Foundation of China (Nos. 22375120 and 21975148), Natural Science Basic Research Program of Shaanxi (No. 2022JC-05), Technology and Innovation Seed Fund (Project CXPY2022092), 111 Project (No. B14041), and International Joint Research Center on Advanced Characterizations of Xi'an City, China.

Conflicts of interest

All authors declared that there are no conflicts of interest.

Ethical approval and consent to participate

Not applicable.

Consent for publication

Not applicable.

Copyright

REFERENCES

1. Zhu, Z.; Jiang, T.; Ali, M.; et al. Rechargeable batteries for grid scale energy storage. *Chem. Rev.* **2022**, *122*, 16610-751. DOI
2. Zhao, Y.; Saseendran, D. P. A.; Huang, C.; et al. Oxygen evolution/reduction reaction catalysts: from in situ monitoring and reaction mechanisms to rational design. *Chem. Rev.* **2023**, *123*, 6257-358. DOI
3. Gao, X.; Chen, Y.; Wang, Y.; et al. Next-generation green hydrogen: progress and perspective from electricity, catalyst to electrolyte in electrocatalytic water splitting. *Nano-Micro. Lett.* **2024**, *16*, 237. DOI PubMed PMC
4. Zhang, H.; Yu, Y.; Yang, D.; et al. Multifunctional quasi-homogeneous catalysts as a new catalytic strategy to boost the performance of Li-O_2 batteries. *Adv. Mater.* **2025**, *37*, 2413948. DOI
5. Yang, B.; Liu, W.; Gu, T.; Wu, Z. Material design and catalyst-membrane electrode interface engineering for high-performance rechargeable zinc-air batteries. *Energy. Storage. Mater.* **2025**, *74*, 103985. DOI
6. Chen, Y.; Wang, G.; Li, J.; et al. Recent advances in bifunctional carbon-based single-atom electrocatalysts for rechargeable zinc-air batteries. *Green. Chem.* **2025**, *27*, 293-324. DOI
7. Wang, Q.; Kaushik, S.; Xiao, X.; Xu, Q. Sustainable zinc-air battery chemistry: advances, challenges and prospects. *Chem. Soc. Rev.* **2023**, *52*, 6139-90. DOI
8. Lv, X. W.; Wang, Z.; Lai, Z.; et al. Rechargeable zinc-air batteries: advances, challenges, and prospects. *Small* **2024**, *20*, e2306396. DOI
9. Yang, Z.; Chen, Y.; Zhang, S.; Zhang, J. Identification and understanding of active sites of non-noble iron-nitrogen-carbon catalysts for oxygen reduction electrocatalysis. *Adv. Funct. Mater.* **2023**, *33*, 2215185. DOI
10. Liu, L.; Rao, X.; Zhang, S.; Zhang, J. Insight into synergy for oxygen reduction electrocatalysis of iron-nitrogen-carbon. *Chem* **2024**, *10*, 1994-2030. DOI
11. Zhang, Z.; Liu, J.; Curcio, A.; et al. Atomically dispersed materials for rechargeable batteries. *Nano. Energy.* **2020**, *76*, 105085. DOI
12. Li, L.; Tang, X.; Wu, B.; Huang, B.; Yuan, K.; Chen, Y. Advanced architectures of air electrodes in zinc-air batteries and hydrogen fuel cells. *Adv. Mater.* **2024**, *36*, 2308326. DOI
13. Lei, H.; Ma, L.; Wan, Q.; et al. Porous carbon nanofibers confined NiFe alloy nanoparticles as efficient bifunctional electrocatalysts for Zn-air batteries. *Nano. Energy.* **2022**, *104*, 107941. DOI
14. Chen, D.; Yu, R.; Yu, K.; et al. Bicontinuous RuO_2 nanoreactors for acidic water oxidation. *Nat. Commun.* **2024**, *15*, 3928. DOI PubMed PMC
15. Yin, S.; Chen, L.; Yang, J.; et al. A Fe-NC electrocatalyst boosted by trace bromide ions with high performance in proton exchange membrane fuel cells. *Nat. Commun.* **2024**, *15*, 7489. DOI PubMed PMC
16. Zhan, Y.; Zhao, T.; Wu, X.; et al. Strengthening the oxygen reduction stability and activity of single iron active sites via a simultaneously electronic regulation and structure design strategy. *Appl. Catal. B. Environ. Energy.* **2024**, *357*, 124254. DOI
17. Liu, J.; Gong, Z.; Allen, C.; et al. Edge-hosted Fe-N_3 sites on a multiscale porous carbon framework combining high intrinsic activity with efficient mass transport for oxygen reduction. *Chem. Catalysis.* **2021**, *1*, 1291-307. DOI
18. Yang, C.; Chen, J.; Yan, L.; Gao, Y.; Ning, J.; Hu, Y. Customizing oxygen electrocatalytic microenvironment with S, N codoped carbon nanofibers confining carbon nanocapsules and Co_9S_8 nanoparticles for rechargeable Zn-air batteries. *Appl. Catal. B. Environ. Energy.* **2024**, *352*, 124060. DOI
19. Chen, K.; Liang, Y.; Pan, D.; et al. Mass transportation facilitated porous Fe/Co dual-site catalytic cathodes for ultrahigh-power-density Al-air fuel cells. *Adv. Energy. Mater.* **2025**, *15*, 2404140. DOI
20. Zhai, W.; Li, J.; Tian, Y.; et al. Consolidating the oxygen reduction with sub-polarized graphitic Fe-N_4 atomic sites for an efficient flexible zinc-air battery. *Nano. Lett.* **2024**, *24*, 14632-40. DOI
21. Zhao, Y.; Zhu, L.; Tang, J.; et al. Enhancing electrocatalytic performance via thickness-tuned hollow N-doped mesoporous carbon with embedded Co nanoparticles for oxygen reduction reaction. *ACS. Nano.* **2024**, *18*, 373-82. DOI
22. Li, J. K.; Zhao, H.; Zhang, Y.; et al. In situ electron tomography insights into the curvature effect of a concave surface on Fe single atoms for durable oxygen reaction. *Adv. Sci.* **2025**, *12*, 2412387. DOI PubMed PMC

23. Zhang, P.; Chen, H. C.; Zhu, H.; et al. Inter-site structural heterogeneity induction of single atom Fe catalysts for robust oxygen reduction. *Nat. Commun.* **2024**, *15*, 2062. DOI PubMed PMC
24. Zhai, X.; Qu, J.; Wang, J.; et al. Diffusion-driven fabrication of yolk-shell structured K-birnessite@mesoporous carbon nanospheres with rich oxygen vacancies for high-energy and high-power zinc-ion batteries. *Energy. Storage. Mater.* **2021**, *42*, 753-63. DOI
25. Song, X.; Zhang, J.; Feng, X.; Qi, Y.; Cui, J.; Xiong, Y. $CoFe_2O_4$/CoFe loaded 3D ordered hierarchical porous N-doped carbon for efficient oxygen reduction in Zn-air battery and hydrogen evolution. *J. Energy. Chem.* **2025**, *106*, 220-30. DOI
26. Zhang, W.; Li, H.; Feng, D.; et al. MOF-derived 1D/3D N-doped porous carbon for spatially confined electrochemical CO_2 reduction to adjustable syngas. *Carbon. Energy.* **2024**, *6*, e461. DOI
27. Wang, Y.; Sun, T.; Mostaghimi, A. H. B.; et al. Two-dimensional metal-organic frameworks with unique oriented layers for oxygen reduction reaction: tailoring the activity through exposed crystal facets. *CCS. Chem.* **2022**, *4*, 1633-42. DOI
28. Chen, R.; Yao, J.; Gu, Q.; et al. A two-dimensional zeolitic imidazolate framework with a cushion-shaped cavity for CO_2 adsorption. *Chem. Commun.* **2013**, *49*, 9500-2. DOI
29. Wang, T.; Kou, Z.; Mu, S.; et al. 2D dual-metal zeolitic-imidazolate-framework-(ZIF)-derived bifunctional air electrodes with ultrahigh electrochemical properties for rechargeable zinc-air batteries. *Adv. Funct. Mater.* **2018**, *28*, 1705048. DOI
30. Shen, J.; Aljarb, A.; Cai, Y.; et al. Engineering grain boundaries in monolayer molybdenum disulfide for efficient water-ion separation. *Science* **2025**, *387*, 776-82. DOI
31. Qin, J.; Yang, Z.; Xing, F.; Zhang, L.; Zhang, H.; Wu, Z. Two-Dimensional mesoporous materials for energy storage and conversion: current status, chemical synthesis and challenging perspectives. *Electrochem. Energy. Rev.* **2023**, *6*, 9. DOI
32. He, J.; Wang, W.; Yan, J.; et al. Stabilizing electron transport of 2D materials. *Adv. Mater.* **2025**, *37*, 2411941. DOI
33. Zhao, B.; Luo, H.; Liu, J.; et al. S-doped carbonized wood fiber decorated with sulfide heterojunction-embedded S, N-doped carbon microleaf arrays for efficient high-current-density oxygen evolution. *Chin. Chem. Lett.* **2025**, *36*, 109919. DOI
34. Fan, Y.; Wang, W.; Chen, Y.; et al. Cobalt-containing ZIF-derived catalysts for Zn-air batteries. *Mater. Chem. Front.* **2024**, *8*, 2394-419. DOI
35. Guo, X.; Zhang, H.; Yao, Y.; et al. Stabilizing atomic Co on 2D ordered mesoporous carbon sandwiched MXene for peroxymonosulfate activation: Enhanced performance and electron-transfer mechanism. *Appl. Catal. B. Environ. Energy.* **2024**, *358*, 124432. DOI
36. Ma, M.; Pei, Z.; Peng, Y.; et al. Single Zn atoms anchored in mesoporous N-doped carbon rods derived from metal-organic frameworks for enhanced electrocatalytic oxygen reduction reaction. *J. Mater. Chem. A.* **2025**, *13*, 7529-38. DOI
37. Huang, Z.; Ma, D.; Nian, P.; et al. Coordinating interface polymerization with micelle mediated assembly towards two-dimensional mesoporous carbon/CoNi for advanced lithium-sulfur battery. *Small* **2023**, *19*, 2207411. DOI
38. Dai, X.; Zhao, Z. ZIF-L-derived $FeN\text{-}_{hc}C$ catalysts with curved carbon surfaces for effective oxygen reduction reaction over the entire pH range. *New. J. Chem.* **2024**, *48*, 18719-27. DOI
39. Xu, Y.; Hou, W.; Huang, K.; et al. Engineering built-in electric field microenvironment of CQDs/g-C_3N_4 heterojunction for efficient photocatalytic CO_2 reduction. *Adv. Sci.* **2024**, *11*, 2403607. DOI
40. Zhang, S.; Wu, J.; Zheng, M.; et al. Fe/Cu diatomic catalysts for electrochemical nitrate reduction to ammonia. *Nat. Commun.* **2023**, *14*, 3634. DOI
41. He, J.; Li, N.; Li, Z.; et al. Strategic defect engineering of metal-organic frameworks for optimizing the fabrication of single-atom catalysts. *Adv. Funct. Mater.* **2021**, *31*, 2103597. DOI
42. Li, W.; Chen, L.; Qiu, M.; et al. Highly efficient epoxidation of propylene with *in situ* -generated H_2O_2 over a hierarchical TS-1 zeolite-supported non-noble nickel catalyst. *ACS. Catal.* **2023**, *13*, 10487-99. DOI
43. Fan, X. Z.; Du, X.; Pang, Q. Q.; Zhang, S.; Liu, Z. Y.; Yue, X. Z. In situ construction of bifunctional N-doped carbon-anchored Co nanoparticles for OER and ORR. *ACS. Appl. Mater. Interfaces.* **2022**, *14*, 8549-56. DOI
44. Chen, Z.; Xu, W.; Wang, W.; et al. Bamboo-like carbon nanotube-encapsulated Fe_2C nanoparticles activate confined Fe_2O_3 nanoclusters via d-p-d orbital coupling for alkaline oxygen evolution reaction. *Small* **2025**, *21*, 2409325. DOI
45. Tang, X.; Wei, Y.; Zhai, W.; et al. Carbon nanocage with maximum utilization of atomically dispersed iron as efficient oxygen electroreduction nanoreactor. *Adv. Mater.* **2023**, *35*, 2208942. DOI
46. Lyu, L.; Hu, X.; Lee, S.; et al. Oxygen reduction kinetics of Fe-N-C single atom catalysts boosted by pyridinic N vacancy for temperature-adaptive Zn-air batteries. *J. Am. Chem. Soc.* **2024**, *146*, 4803-13. DOI
47. Zhu, Y.; Jiang, Y.; Li, H.; et al. Tip-like Fe-N_4 sites induced surface microenvironments regulation boosts the oxygen reduction reaction. *Angew. Chem. Int. Ed.* **2024**, *63*, e202319370. DOI
48. Wang, Y.; Yang, T.; Fan, X.; et al. Anchoring Fe species on the highly curved surface of S and N Co-doped carbonaceous nanosprings for oxygen electrocatalysis and a flexible zinc-air battery. *Angew. Chem. Int. Ed.* **2024**, *63*, e202313034. DOI
49. Sang, W.; Chaemchuen, S.; Zhang, L.; et al. Solid-state stepwise temperature-programmable synthesis of bioinspired Fe-N-C oxygen reduction electrocatalyst featuring Fe-N_5 configuration. *Nano. Res.* **2025**, *18*, 94907245. DOI
50. Bae, G.; Kwon, H. C.; Han, M. H.; Oh, H.; Jaouen, F.; Choi, C. H. Single-site-level deciphering of the complexity of electrochemical oxygen reduction on Fe-N-C catalysts. *ACS. Catal.* **2024**, *14*, 8184-92. DOI
51. Jia, C.; Zhao, Y.; Song, S.; et al. Highly ordered hierarchical porous single-atom Fe catalyst with promoted mass transfer for efficient electroreduction of CO_2. *Adv. Energy. Mater.* **2023**, *13*, 2302007. DOI
52. Liu, S.; Meyer, Q.; Jia, C.; et al. *Operando* deconvolution of the degradation mechanisms of iron-nitrogen-carbon catalysts in proton

exchange membrane fuel cells. *Energy. Environ. Sci.* **2023**, *16*, 3792-802. DOI

53. Liu, Y.; Li, J.; Lv, Z.; et al. Efficient proton-exchange membrane fuel cell performance of atomic Fe sites via p-d hybridization with Al dopants. *J. Am. Chem. Soc.* **2024**, *146*, 12636-44. DOI
54. Wang, X.; Zhang, J.; Wang, P.; et al. Terbium-induced cobalt valence-band narrowing boosts electrocatalytic oxygen reduction. *Energy. Environ. Sci.* **2023**, *16*, 5500-12. DOI
55. Li, J.; Zhu, Y.; Chen, W.; et al. Breathing-mimicking electrocatalysis for oxygen evolution and reduction. *Joule* **2019**, *3*, 557-69. DOI
56. Jiang, S.; Xiang, Q.; Xie, Z.; et al. Influence of the Pt/ionomer/water interface on the oxygen reduction reaction: insights into the micro-three-phase interface. *Chem. Sci.* **2024**, *15*, 19290-8. DOI PubMed PMC
57. Yan, L.; Xie, B.; Yang, C.; et al. Engineering self-supported hydrophobic-aerophilic air cathode with CoS/Fe_3S_4 nanoparticles embedded in S, N Co-doped carbon plate arrays for long-life rechargeable Zn-air batteries. *Adv. Energy. Mater.* **2023**, *13*, 2204245. DOI
58. Zhao, Y.; Shi, Z.; Li, F.; et al. Deciphering mesopore-augmented CO_2 electroreduction over atomically dispersed Fe-N-doped carbon catalysts. *ACS. Catal.* **2024**, *14*, 3926-32. DOI
59. Wu, J.; Zhu, Y.; Cai, A.; Fan, X.; Peng, W.; Li, Y. Structural engineering of Fe single-atom oxygen reduction catalyst with high site density and improved mass transfer. *J. Energy. Chem.* **2024**, *98*, 634-44. DOI
60. Li, S.; Peng, X.; Wang, C.; Zhao, X.; Dang, J.; Li, J. Confinement effects boosted oxygen reduction reactions inside FeN_4-decorated carbon nanotubes. *Chem. Catal.* **2024**, *4*, 101059. DOI